OPEN

A silicon carbide-based highly transparent passivating contact for crystalline silicon solar cells approaching efficiencies of 24%

Malte Köhler [1,2 ✉], Manuel Pomaska [1 ✉], Paul Procel[3,4], Rudi Santbergen[3], Alexandr Zamchiy [5,6], Bart Macco[7], Andreas Lambertz[1], Weiyuan Duan[1], Pengfei Cao[8], Benjamin Klingebiel[1], Shenghao Li [1], Alexander Eberst [1,2], Martina Luysberg[8], Kaifu Qiu [1,9 ✉], Olindo Isabella [3], Friedhelm Finger[1], Thomas Kirchartz [1,10], Uwe Rau [1,2] and Kaining Ding [1 ✉]

A highly transparent passivating contact (TPC) as front contact for crystalline silicon (c-Si) solar cells could in principle combine high conductivity, excellent surface passivation and high optical transparency. However, the simultaneous optimization of these features remains challenging. Here, we present a TPC consisting of a silicon-oxide tunnel layer followed by two layers of hydrogenated nanocrystalline silicon carbide (nc-SiC:H(n)) deposited at different temperatures and a sputtered indium tin oxide (ITO) layer (c-Si(n)/SiO$_2$/nc-SiC:H(n)/ITO). While the wide band gap of nc-SiC:H(n) ensures high optical transparency, the double layer design enables good passivation and high conductivity translating into an improved short-circuit current density (40.87 mA cm^{-2}), fill factor (80.9%) and efficiency of 23.99 $\pm$ 0.29% (certified). Additionally, this contact avoids the need for additional hydrogenation or high-temperature postdeposition annealing steps. We investigate the passivation mechanism and working principle of the TPC and provide a loss analysis based on numerical simulations outlining pathways towards conversion efficiencies of 26%.

At present, the efficiency of most crystalline silicon (c-Si) solar cells is limited by recombination in the diffused emitter regions and at the contact between metal electrodes and the silicon absorber[1]. Device designs that avoid diffused emitter regions and direct metal-absorber contacts, commonly denoted as passivated contacts, are key enablers for a further increase of efficiency. So far, three concepts have been developed that enable junction formation in crystalline silicon solar cells without diffused emitters. These concepts are: the silicon heterojunction (SHJ) based on intrinsic and doped amorphous silicon[2-4]; the so-called TOPCon or POLO concepts using a combination of silicon oxide and polycrystalline silicon (SiO$_2$/poly-Si)[5,6] and the use of metal oxides/nitrides/fluorides such as MoO$_x$ (refs. [7–9]), TiN[10] or LiF[8].
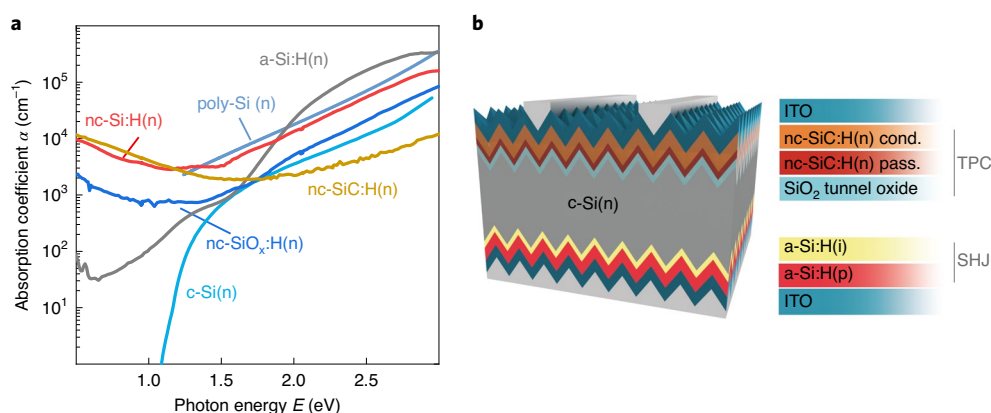
While these approaches allow high efficiencies, they come with a considerable drawback. The implementation of, for example, MoO$_x$ combined with intrinsic hydrogenated amorphous silicon (a-Si:H) enabled solar cells with an efficiency >23.5% (ref. [11]). The short-circuit current density (J_{sc}) limited the efficiency due to the high amount of parasitic absorption by the intrinsic a-Si:H layer. The other two concepts have achieved efficiencies in the >25% range so far. However, due to the low band gaps and substantial absorption coefficients of a-Si:H and poly-Si (Fig. 1a), these layers cause stronger parasitic absorption losses when compared to other nanocrystalline silicon/silicon alloys with comparable thickness but

a higher band gap. In the case of poly-Si, these optical losses are so severe that the application of this contact is up to now restricted to the rear side of c-Si solar cells[12]. It can also be clearly seen in Fig. 1a that for photon energies above 1.75 eV, nc-SiC:H(n) features the lowest absorption coefficient and thereby the best transparency among these materials.

While nc-SiC:H(n) is an obvious candidate to achieve highly transparent front contacts, so far efficiencies have lagged behind due to difficulties in obtaining nc-SiC:H(n) that features high transparency, good conductivity and at the same time provides sufficient hydrogenation for passivation. These three properties are the challenges to be overcome for high efficiency c-Si solar cells, as depicted in Supplementary Note 1 in the Supplementary Information.

The present paper demonstrates how to overcome this drawback by using exclusively low-temperature processes and by the implementation of a highly transparent passivating contact (TPC) scheme consisting of a thin, wet-chemically grown SiO$_2$ tunnel oxide and a hot-wire chemical vapour deposition (HWCVD) fabricated wide band gap nc-SiC:H(n) (E_g of approximately 2.7–3 eV)[13] contact layer, as depicted in Fig. 1b. Here, we demonstrate an independently confirmed efficiency of 23.99 $\pm$ 0.29%. This efficiency was achieved by introducing a double layer stack of nc-SiC:H(n) deposited first with low and subsequently with high filament temperatures to tackle the trade-off between passivation and conductivity.

Fig. 1 | Motivation and concept of the TPC. a, The in-house measured absorption coefficient of nc-SiC:H(n), nc-Si:H(n), nc-SiO$_x$:H(n), a-Si:H(n) and poly-Si(n) used in existing passivating contacts. A reference absorption coefficient of c-Si is included[53]. The nanocrystalline silicon/silicon alloys exhibit pronounced free-carrier absorption at low photon energies due to the high doping density. **b**, Sketch of a silicon solar cell using an n-type wafer with a TPC on front side using our developed nc-SiC:H(n)/SiO$_2$ stack. Considering the high sheet resistance (approximately $10^6\,\Omega\,\mathrm{sq}^{-1}$) of the nc-SiC:H(n), an additional ITO layer with a sheet resistance of approximately $200\,\Omega\,\mathrm{sq}^{-1}$ is used for lateral transport. The back side consists of intrinsic and p-type hydrogenated amorphous silicon (a-Si:H(i/p)) and an ITO layer.

Furthermore, a systematic investigation and optimization of the ITO sputtering conditions combined with a low-temperature curing contributed to the efficiency improvement.

Development of a nc-SiC:H(n) double layer stack

For nc-SiC:H(n) deposited at low filament temperatures ($T_f < 1,750\,°C$), the electrical conductivity is usually below $10^{-10}\,\mathrm{S\,cm^{-1}}$ compared to filament temperatures between 1,900 and 2,100 °C where the electrical conductivity drastically increases to $0.07–0.9\,\mathrm{S\,cm^{-1}}$ (see Supplementary Note 2 for more information about the electrical properties of nc-SiC:H(n)). Given that the higher band gap of nc-SiC:H(n) is a natural advantage in terms of optical transparency, the optimization of the nc-SiC:H(n) layer still has to tackle the trade-off between passivation and conductivity that hampered earlier attempts to make efficient silicon solar cells with SiC-based contacts[13,14].

Figure 2 shows the implied open-circuit voltage (iV_{oc}) of the c-Si(n) wafer symmetrically passivated by the TPC (Fig. 2a) and the contact resistivity of the TPC stack (Fig. 2b) as a function of the filament temperature. For a single nc-SiC:H(n) layer (thickness of 30 nm) deposited at increased filament temperatures the passivation quality of the TPC is reduced, while high T_f is needed for low contact resistivities (Fig. 2b). Thus, a single nc-SiC:H(n) layer deposited by HWCVD cannot maximize passivation quality and minimize resistive losses at the same time. To overcome this trade-off, the filament temperature during the deposition was changed, hence a double layer stack of nc-SiC:H(n) was implemented (9 nm for the first layer and 25–30 nm for the second layer). The modified process starts with a lower T_f of 1,775 °C for the layer in direct contact with the tunnel oxide. This is followed by a layer deposited using a higher T_f, which was initially varied as shown in Fig. 2a. This double layer nc-SiC:H(n) stack allows to keep the passivation quality nearly independent of T_f in the second stage resulting in a maximum iV_{oc} of 740 mV. At the same time, the contact resistivity is kept at a low value of 38 mΩ cm², as shown in Fig. 2b. Achieving the same low contact resistivity in a single layer would cause a substantial loss in passivation quality ($iV_{oc} < 720$ mV).

Three mechanisms presumably contribute to the reduced iV_{oc} at higher T_f. First, the nc-SiC:H(n) deposited at higher T_f contains less hydrogen than at lower T_f. However, hydrogen is necessary to passivate remaining dangling bonds at the c-Si/SiO$_2$ interface. Second, the substrate temperature is increased due to increased thermal radiation of the filaments at increased T_f. An increased substrate temperature is known to reduce the TPC passivation quality[15], which might be caused by an out-diffusion of hydrogen from the interface. Third, higher T_f leads to an increased hydrogen radical density during the HWCVD deposition[16]. The hydrogen radicals can be a source of damage for the crystalline silicon interfaces[17,18], thus increase the density of dangling bonds and deteriorate the passivation quality.

In addition to the filament temperatures, the thicknesses of both nc-SiC:H(n) layers and the doping gas flow might also be factors influencing passivation quality and conductivity. To be able to judge which deposition parameters have the strongest influence on the overall solar cell performance, we conducted a design of experiment (DoE). In this DoE we found that the thickness of the first nc-SiC:H(n) layer for passivation with low electrical conductivity has the strongest influence on the fill factor. By decreasing the thickness from 13 to 3 nm to decrease the bulk resistance, the series resistance was reduced from 2.5 to 0.65 Ω cm² resulting in a fill factor increase from 63 to 77% while maintaining the high passivation quality (see Methods and Supplementary Discussion 1 for more details about the DoE).

Passivation mechanism and working principle of TPC

In contrast to SiO$_2$/poly-Si passivating contacts, the passivation of SiO$_2$/nc-SiC:H(n) works without any high-temperature recrystallization, hydrogenation or firing steps[19]. The as-deposited low-temperature (heater set temperature of 250 °C) nc-SiC:H(n) deposited by HWCVD was found in literature to allow for an effective interface hydrogenation for c-Si(n)/SiO$_2$/poly-Si contacts without additional steps[20]. Since no high-temperature steps are involved in the TPC fabrication process, the hydrogen supplied during HWCVD deposition is also found to accumulate at the c-Si(n)/SiO$_2$ interface. This effect can be seen in Fig. 3a displaying the secondary-ion mass spectrometry (SIMS) profiles. This hydrogen avoids the demand of any further hydrogenation steps. For the single layer stack shown in the upper graph of Fig. 3a, the hydrogen concentration in the nc-SiC:H(n) bulk is decreased for increased T_f, while the hydrogen concentration at the interface is increased. The reason for the accumulation of hydrogen at the interface is most probably the increased sample temperature as higher thermal radiation of the hot wires enables a higher diffusivity of the hydrogen. Another potential reason for the accumulation is that the higher
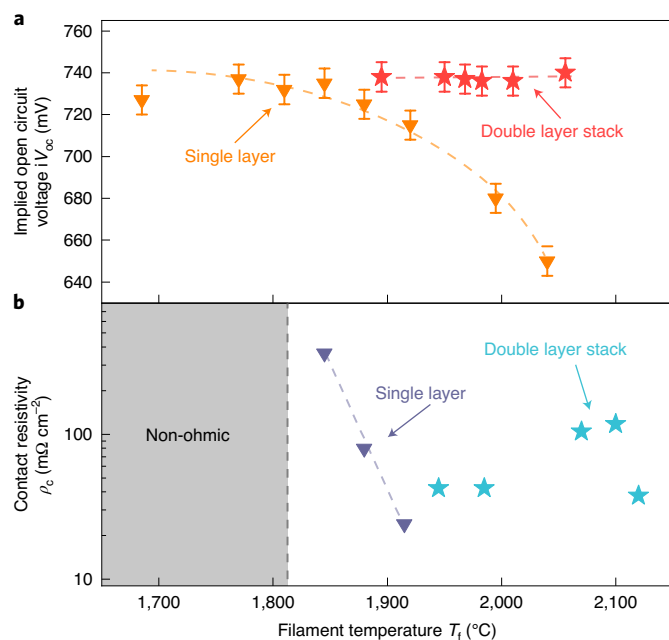
Fig. 2 | Selectivity of the TPC. a,b, Implied open-circuit voltage (iV_{oc}) of the n-type Si wafer (170 μm, 1 Ω cm) symmetrically passivated by the TPC (**a**) and contact resistivity (ρ_c) for the whole TPC stack (**b**) as a function of the hot-wire filament temperature (T_f). For contact resistivity measurements, a second set of samples was used, which had a patterned ITO layer with the same size as the Ag electrode on top of the nc-SiC:H(n). The inverted triangles show the results for a single nc-SiC:H(n) layer (thickness of 30 nm) stack. Stars show the results for double nc-SiC:H(n) layer (thickness of 9 + 25–30 nm) stack, where T_f of the passivation layer is fixed at 1,775 °C and T_f for the conductive layer is varied according to the x axis. The vertical error bars represent the standard error for each measurement in the photo-conductance measurement. The grey box marks the area where the contact resistivity could not be evaluated due to non-ohmic behaviour of the measured data in the case of single nc-SiC:H(n) layers. One sample was used for each data point in the iV_{oc} and ρ_c measurement. Dashed lines are guides to the eye.

filament temperature also leads to higher kinetic energies of the hydrogen radicals causing deeper in-diffusion. For $T_f = 2,040$ °C, the hydrogen peak at the interface decreased indicating out-diffusion of hydrogen. This behaviour of hydrogen in- and out-diffusion was also reported for SiO_2/poly-Si contacts[21].

Another reason for the high passivation quality is that the SiO_2 layer is working as a protection layer against the hostile deposition conditions during the HWCVD process. The SiO_2 prevents interface damage and simultaneously reduces the dangling bond density at the c-Si(n) surface[22]. The interface of c-Si(n)/SiO_2/nc-SiC:H(n) is undamaged, which is revealed in the high-resolution, bright-field scanning transmission electron microscopy (HRSTEM) image in Fig. 3b. Close to the SiO_2/c-Si interface, the SiC layer is amorphous, whereas nc-SiC crystals embedded in an amorphous matrix are observed in the bulk of the material (Fig. 3b, arrow). The energy dispersive X-ray spectroscopy (EDX) line profile, obtained at a comparable location within the sample, additionally shows that aside from silicon, oxygen is present at the interface to the crystalline silicon substrate, indicating that the SiO_2 is not entirely removed during the HWCVD process (see also the EDX mapping result in Supplementary Fig. 7).

The passivation of the c-Si(n)/SiO_2 interface is additionally supported by the electrostatic potential difference between c-Si(n) and the conductive nc-SiC:H(n). This potential difference induces a

band bending in the c-Si(n) as illustrated in the Fig. 3c showing the band diagram obtained from the technology computer-aided design (TCAD) Sentaurus simulations (Methods and Supplementary Discussion 2). The energy of the Fermi level of nc-SiC:H(n) was measured to be approximately 3 eV relative to the vacuum level (Supplementary Fig. 12). For the conductive nc-SiC:H(n) deposited at higher T_f, the carrier concentration is higher and thus leads to a Fermi level closer to the conduction band, which induces a stronger band bending in the c-Si. Due to the strong band bending in the c-Si, the energy bands can become degenerated close to the c-Si/SiO_2 interface, which induces a strong accumulation of majority charge carriers (electrons) at the interface, while the band bending suppresses the minority charge carrier (holes) accumulation near the c-Si(n)/SiO_2 interface. The concentration difference between the majority and minority carriers at the interface reduces the probability of surface recombination[23]. With a carrier accumulation at the c-Si/SiO_2 interface estimated to be 7.4×10^{19} cm^{-3} from the TCAD simulation, the carrier accumulation exceeds the density of states in the conduction band of c-Si(n) (2.8×10^{19} cm^{-3}). Note that this is achieved without the support of any buried diffusion of dopants in the c-Si(n) as in the case of passivating contacts based on poly-Si[24,25].

Due to the co-existence of the high hydrogen concentration at the c-Si(n)/SiO_2 interface and the strong field-effect passivation, the passivation quality of the SiO_2/nc-SiC:H(n) contact reaches an iV_{oc} up to 740 mV. The stronger band bending and thereby stronger field-effect passivation explains the lower hydrogen content at the interface but similar passivation quality that is found in the double layer stack with the conductive nc-SiC:H(n) deposited at higher T_f (visualized in the lower graph of Fig. 3a). The accumulation of electrons at the c-Si(n) interface promotes the tunnelling through the thin SiO_2 layer to the conductive nc-SiC:H(n) layers. In this respect, the measured activation energy of the dark conductivity is 50 to 100 meV (refs. [15,26]), which represents the energy difference between the conduction band edge and the Fermi level. Such a low value reveals the negligible contribution of nc-SiC:H(n) to the potential barrier for collecting electrons. Hence, TPCs based on nc-SiC:H(n) enable excellent energy alignment for an efficient field-effect passivation and for electron extraction.

The SiC-based tunnel-junction front contact has some comparable properties to the common low-temperature approach of the a-Si SHJ double stack (doped/intrinsic). These similarities include the supply of H_2 to the interface by the intrinsic/passivation layer, field-effect passivation and carrier selectivity provided by the doped/conductive layer. The key difference lies in the absence of the smaller band gap and the low transparency of the doped a-Si or even poly-Si layers relative to the nc-SiC:H(n). Additionally, using the tunnel oxide rather than intrinsic a-Si:H as the interface passivation layer on top of the c-Si, the TPC further facilitate the advantage in terms of transparency.

Investigation and mitigation of sputter degradation

On completion of the devices we observed a substantial difference between the implied V_{oc} after nc-SiC:H(n) deposition and the actual V_{oc} of the finished devices. This difference of up to 32 mV indicates that during ITO sputtering the passivation quality is substantially deteriorated, which is similar to that reported for solar cells passivated by a-Si:H[27] and SiO_2/poly-Si[28,29]. Degradation of the passivation due to ITO sputtering can originate either from ion bombardment or from ultraviolet (UV) light emitted for example by oxygen in the plasma ($\lambda = 130.5$ nm) during sputtering[30,31].

To identify the main source of the sputter degradation, we conducted model experiments measuring the minority charge carrier lifetime of wafers that were symmetrically passivated by TPC. The wafers were partially covered with different optical filters and exposed either to a pure oxygen plasma without sputtering or a complete ITO deposition process (see details in Supplementary
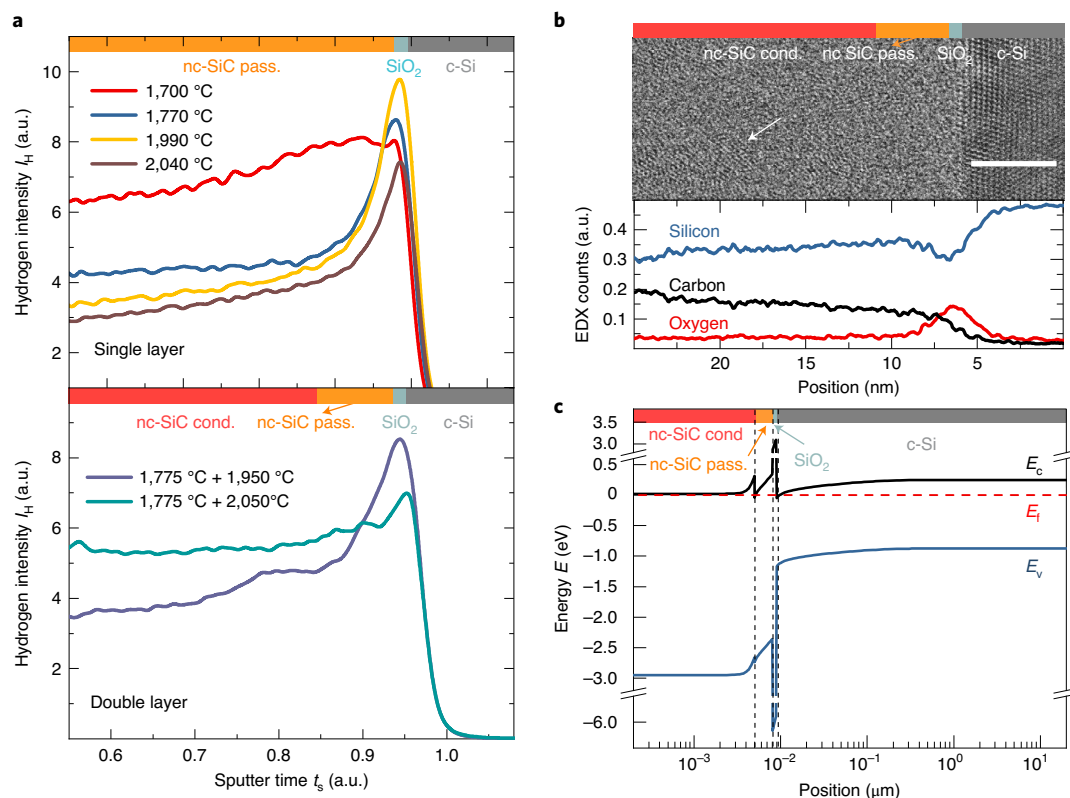
Fig. 3 | Passivation mechanism and working principle of the TPC. a, The SIMS profiles of hydrogen as a function of the sputter time for the single nc-SiC:H(n) layer stack (thickness of 30 nm, upper graph) and double nc-SiC:H(n) layer stack (thickness of 3 + 30 nm, lower graph) prepared at different filament temperatures (T_f). The same substrate and tunnel oxide are used for all samples. For the double nc-SiC:H(n) layer, the T_f is kept at 1,775 °C for the first layer. a.u., arbitrary units. **b**, HRSTEM bright-field image and EDX measurement of the c-Si(n)/SiO$_2$/nc-SiC:H(n) interface. The arrow is to show the SiC crystallites embedded in an amorphous matrix. The EDX line profile is obtained at a similar location, which clearly shows the oxygen presence at the interface to the silicon substrate. Scale bar, 5 nm. **c**, Energy band diagram in equilibrium of the hetero-interface comprising c-Si(n) bulk and SiO$_2$/nc-SiC:H(n) stack (vertical grey dashed lines). E_c (black solid line) is the conduction band energy; E_v (blue solid line) is the valence band energy and E_f (red dashed line) is the Fermi level.

Discussion 3). During the pure plasma treatment, only those areas that were covered with filters blocking wavelengths down to 130 nm radiation preserved a high lifetime. In contrast, during ITO deposition all areas that were covered by any filter, blocking or partly transparent to the 130 nm radiation, preserved a high minority charge carrier lifetime due to the physical protection of the wafer from sputter damage. Furthermore, the uncovered areas showed only a moderate degradation compared to the results from the pure plasma experiment. We therefore conclude that during the deposition process the damage by radiation is increasingly limited by the optical transparency of the growing ITO film and the sputter damage is the relevant degradation mechanism to be considered.

This finding indicates that an optimization of the ITO deposition process by adjusting the ion flux density by the sputter power (P_{dep}) and the secondary-ion energy by the deposition pressure (p_{dep}) is required. For the latter, a higher pressure reduces the free path and therefore reduces the kinetic energy of the ions. The best solar cell with the optimized ITO sputtering process showed an increase in V_{oc} with respect to the reference from 711 to 718 mV. However, the difference from before sputtering to after sputtering (iV_{oc} to V_{oc}) is still 20 mV.

As a final measure, we cured the samples on a hot plate in two steps at 220 °C for 10 + 10 min leading to an improvement in V_{oc} by 4 and 7 mV for the two cells with improved (high pressure, low power) and optimum (high pressure, intermediate power) deposition conditions. In contrast, the reference cell exhibited no increase in V_{oc} by the same treatment. The highest V_{oc} in this series was 725 mV going along with the lowest iV_{oc} to V_{oc} difference (before sputtering to after curing) of 12 mV. Thus, lowering ion energy and flux not only reduces the initial damage but also allows some of the damage to be cured, for example by the reduction of dangling bonds at the interface due to the re-organization of hydrogen[32].

Optical loss analysis for the optimized solar cell

The performance of the four best solar cells after the curing experiment (Supplementary Fig. 16) were independently certified by CalTeC at the Institute for Solar Energy Research in Hamelin (Supplementary Fig. 17 and Supplementary Discussion 4). The best solar cell of this series was certified with an efficiency of 23.79% and a V_{oc} of 725 mV. Subsequently, a MgF$_2$ layer was used as an antireflection coating to reduce the reflectivity of the solar cells (Supplementary Fig. 18) leading to a certified efficiency $\eta = 23.99 \pm 0.29\%$ and $J_{sc} = 40.87 \pm 0.57$ mA cm^{-2} (Supplementary Fig. 19). The evolution of the solar cell parameters due to the optimization of the SiC double layer, transparent conductive oxide (TCO) and ARC is summarized in Fig. 4. For comparison, µc-SiO$_x$:H(p) as a front side emitter layer allowed for $J_{sc} = 40.4$ mA cm^{-2} but with much lower V_{oc} and fill factor, FF (ref. [33]). Implementing a double layer antireflection coating of SiO$_x$:H/ITO for SHJ solar cells yielded a $J_{sc} = 40.6$ mA cm^{-2} via a photolithography based metallization[34]. Within the measurement error range, our result equals the short-circuit current density record value of 40.8 mA cm^{-2} for a both-side-contacted SHJ solar cell
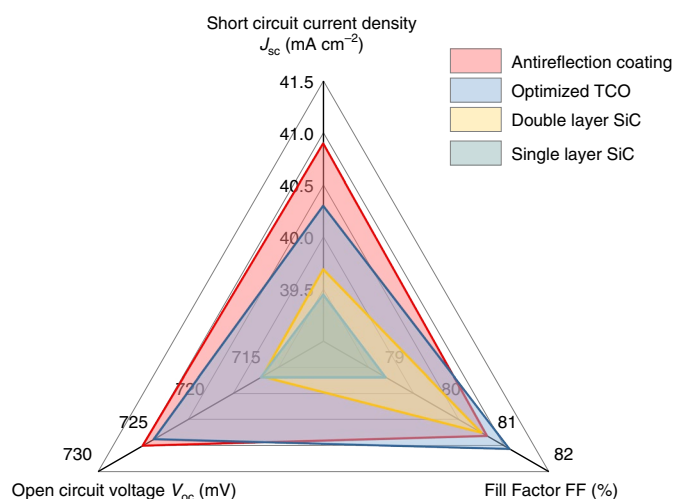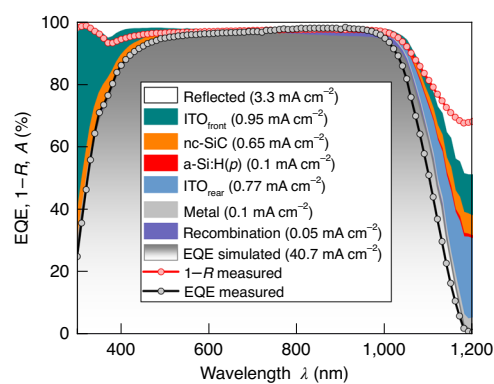
Fig. 4 | Illustration of the evolution of TPC solar cells. Evolution of the TPC IV parameters from single layer to the double layer, the optimized ITO deposition, and the improvement due to MgF$_2$ antireflection coating. The optimization of the TPC solar cells is along these triangle points. All solar cells have been measured with isolated back contacts of the surrounding cells (more details about the measurement are in Supplementary Discussion 4).

Fig. 5 | Optical loss analysis of the optimized TPC solar cell. The optimized front contact stack includes 70 nm of ITO, 30 nm of conductive nc-SiC:H(n) and 3 nm of passivating nc-SiC:H(n). A shading loss due to front contact metal fingers and the ARC of 125 nm of MgF$_2$ are taken into consideration in the simulation. The legend indicates each optical part, with the integration current density shown in brackets. The EQE and optical losses (reflectance R and absorbtance A) are simulated using GenPro4. The real EQE is calculated from the spectral response data certificated at CalTec ISFH.

reported by Kaneka[35]. Here, Kaneka used the copper plating technology for metallization and a finger width of approximately 30–40 µm (refs. [35,36]). However, due to the lack of information concerning the metallization fraction and ARC of this solar cell, we cannot provide an in-depth comparison. For our cells, we used a finger width of approximately 60 µm and a circumferential busbar outside of the active area (Supplementary Fig. 20).

The optimized front contact stack includes 70 nm of ITO, 30 nm of conductive nc-SiC:H(n) and 3 nm of passivating nc-SiC:H(n). By performing an optical simulation with the software GenPro4 (ref. [37]), we present the optical analysis of the optimized solar cells in Fig. 5. The simulations are performed for the device (coated with a 125 nm MgF$_2$ layer) shown in Supplementary Fig. 19. For the relevant wavelength range (300–1,100 nm) there is a good agreement between measured and simulated results. Only for wavelengths longer than 1,100 nm are the deviations between simulation and measurement substantial. This can most probably be explained by an underestimation of the absorption coefficient of the TCO or silver in this wavelength range. Since in this wavelength range the absorptance of c-Si is negligible, this optical deviation does not affect the calculated optical generation rate or the subsequent electrical simulations based on these optical simulations.

The shading of the grid of 3.1% leads to a short-circuit current density loss of 1.4 mA cm^{-2}. The parasitic absorption in the nc-SiC:H(n) layers is less than 0.7 mA cm^{-2}, thus confirming the high transparency. In contrast, >2 mA cm^{-2} is typically lost by parasitic absorption in the front side layer stack of conventional front-back contacted SHJ solar cells[38]. This result was experimentally validated by measurements on SHJ cells made in-house[39] and by state-of-the-art SHJ cells from Kaneka[40]. Moreover, the high passivation quality leads to recombination losses of less than 0.05 mA cm^{-2}. The highest parasitic absorption loss is introduced by the front side ITO. To further increase the J_{sc}, several options can be implemented: decreasing the finger width from currently 60 to 40 µm by using a screen with narrower finger openings; using a thinner ITO and/or more transparent TCO with less parasitic absorption; or implementing a TCO-free concept, where the c-Si(n) wafer with an estimated sheet resistance 60 Ω sq^{-1} supports the

lateral transport of the charge carriers. Removing the TCO, meanwhile, can mitigate sputtering damage due to the TCO deposition, which would also improve the passivation of the contact. The work on a TCO-free contact is currently ongoing.

Practical efficiency potential for TPC solar cells

The theoretical efficiency (η^{theo}) limit for a c-Si solar cell according to Richter et al.[41], which considers the intrinsic limitation and relies on the assumption of a perfect Lambertian light trapping scheme, is predicted to be $\eta^{theo} = 28.66\%$. In the calculation, a 170-µm-thick c-Si wafer with a resistivity of 1 Ω cm as also used in this work is assumed, leading to a theoretical V_{oc}, $V_{oc}^{theo} = 746.9$ mV, theoretical J_{sc}, $J_{sc}^{theo} = 43.72$ mA cm^{-2} and theoretical FF, FF$^{theo} = 87.75\%$. The difference between the theoretical limit of $\eta^{theo} = 28.66\%$ and the actual achieved efficiency in this work of $\eta^{act} = 23.99\%$ is 16.3% relative. Among the IV parameters, the FF shows the strongest potential for improvement with 7.8%, while for J_{sc} the potential is 6.5% and for V_{oc} it is 2.9%.

To investigate the reason for the FF difference, we conducted a FF loss analysis[42] using a two-diode equivalent circuit to model the solar cell. For this analysis, the losses in FF are parameterized by the losses due to the saturation current density of the first and second diode (J_{01} and J_{02}), as well as by the shunt resistance (R_{sh}) and the series resistance (R_s). The saturation current density J_{01} describes recombination currents in the quasi-neutral bulk and the solar cell surfaces, while J_{02} mostly describes the recombination attributed to Shockley–Read–Hall defects in the space charge region. The results are presented in Fig. 6. The maximum FF for our optimized solar cells by avoiding all J_{02}, R_s and R_{sh} related losses is the FF$_{J01}$ and is calculated to be approximately 85%. From the FF loss analysis, it becomes clear that the shunt resistance does not contribute any notable loss to the FF. The loss due to the series resistance is the largest loss (2.96%$_{abs}$) followed by the loss of 1.11%$_{abs}$ due to recombination in the space charge region (J_{02}). The transmission line method (TLM) measurement for the front TPC (ITO/nc-SiC:H(n)/SiO$_2$/c-Si(n)) and the rear SHJ contact (ITO/a-Si:H(p/i)/c-Si(n)) delivers contact resistivities of 38 and 350 mΩ cm^2, respectively, indicating that the rear SHJ contact contributes most strongly to the series resistance and is the bottleneck for FF improvement, which is consistent with the TCAD simulation results.
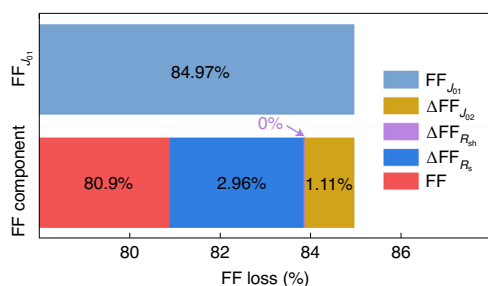
Fig. 6 | Fill factor loss analysis of the optimized TPC solar cell. In this loss analysis, the two-diode model of solar cells is used, which includes two diodes with saturation current densities J_{01}, J_{02} and ohmic resistors R_s, R_{sh} in series and shunt to the diodes, respectively. The stack in red is the actual FF (80.9%) of the optimized solar cells, the stacks represent the FF loss due to the series resistance (2.96%, in blue), the shunt resistance (0%, in purple) and the J_{02} recombination (1.11%, in yellow), respectively. The stack in blue shows the FF assuming the absence of R_s, R_{sh} and J_{02}.

From the Suns-V_{oc} measurement for the optimized solar cells, an R_s of 0.58 Ω cm² can be determined. Using an anticipated value of 0.45 Ω cm² by optimizing the contact resistivity at the rear SHJ contact, a FF of 81.5% can be calculated. Concerning the J_{sc} loss, it is shown in the last section, that the shading loss and parasitic absorption in the ITO are the two biggest losses that need further optimization. By reducing the finger width from 60 to 40 μm (shading ratio from 3.1 to 2.1%), a J_{sc} gain of 0.46 mA cm⁻² can be calculated. Combining this gain with the optimization of the transparency of TCO and reflection minimization, a J_{sc} of 42 mA cm⁻² is practically achievable. Considering that there is still an iV_{oc} to V_{oc} drop of 12 mV, further optimization on improving the iV_{oc} and decreasing the iV_{oc} to V_{oc} drop are important for a higher V_{oc}. The optimization of the SiO₂ preparation process is ongoing. First results show that a 7 mV gain in iV_{oc} is possible, which indicates that a V_{oc} of 730 mV is in reach. An efficiency of 25% can finally be predicted assuming the practical IV parameters of V_{oc} of 730 mV, J_{sc} of 42 mA cm⁻² and FF of 81.5%.

Numerical simulations are performed using the TCAD Sentaurus to identify directions and potentials for further improving the power conversion efficiency of solar cells using the TPC. The results reveal that optimizing the rear SHJ contact stack the V_{oc} and FF could be improved up to 739 mV and 84.2%, respectively. Such an improvement would be due to the field-effect passivation in case of V_{oc} and interface transport in case of FF enhancement[24,43]. Furthermore, considering advanced metallization techniques, for example copper plating, we have the flexibility to have smaller pitch sizes and front metallization fraction. Addressing these two aspects could potentially lead to FF improvements up to 85% due to the decreased lateral transport in the smaller finger pitch (500 μm pitch size and 10 μm front contact width), and J_{sc} above 42 mA cm⁻² due to the smaller metallization fraction (<2% front metallization). In fact, front and back contacted solar cells using TPC technology will be promising candidates to break the 26% threshold for c-Si single junction solar cells.

Conclusion

The present paper has demonstrated that a promising front passivating contact system (SiO₂/nc-SiC:H(n)/ITO) provides a possibility to solve the triple challenge of conductivity, passivation, and transparency. The evolution of TPC solar cells and simulations demonstrate that the SiC-based TPC has an inherent, not yet fully exploited, advantage over other heterojunction contacts in terms of transparency (J_{sc}) with the potential to achieve J_{sc} in the range of

42 mA cm⁻² likes diffused junctions[13]. At the same time, the high V_{oc} of the heterojunctions can be maintained. Thus, innovations such as the double layer nc-SiC:H(n) stack allow to optimize all three photovoltaic parameters without the need of compromising between them. In addition, we demonstrate that the process flow for the TPC is very lean, the extra hydrogenation or high-temperature postdeposition annealing steps, which add cost and energy to the process flow of other passivated contact schemes[44], are not needed. Finally, in view of the short research history, we see scope for further improvements beyond the present efficiency of 24% to a practical efficiency of 25%. Numerical simulations predict an efficiency of 26% by improving FF and V_{oc} via optimizing the SHJ contact at the rear side and introducing a frontier metallization approach such as copper plating.

Methods

Fabrication of symmetric samples and solar cells with TPC. The symmetric samples and solar cells were fabricated with Czochralski grown n-type double-side textured, 170-μm-thick, 1 Ω cm wafers produced by LONGi. The wafers were cleaned in a cleanroom according to standard RCA cleaning[45]. The native oxide was afterwards removed in 1% diluted hydrofluoric acid for 5 min. Afterwards, the wet-chemical oxide was produced in a mixture of H₂O₂:H₂SO₄ at 2:1 at a temperature of around 60 °C for 10 min. This results in a SiO₂ thickness of roughly 1 nm (ref. [46]). The nc-SiC:H(n) layers were deposited by HWCVD partly in an in-house built system and partly in a commercial system built by MRG. As precursors 5% monomethylsilane diluted in H₂ (MMS, 6 standard cubic centimeters per minute (sccm)), hydrogen (H₂, 94 sccm) and nitrogen (N₂, 30 sccm) were used if not stated otherwise. As a catalyser, three 15 cm curled rhenium wires were used. The substrate is heated by a substrate heater set to 250 °C. The deposition pressure was 0.75 mbar. The filament temperature was tuned by adjusting the electrical current through the wires. For double layer stacks, the temperature of the hot-wire filaments was ramped up during the deposition. For symmetric samples, the first layer of nc-SiC:H(n) was deposited at $T_f = 1{,}775$ °C with a thickness of 9 nm. The filament temperature for producing the conductive second layer was varied between $T_f = 1{,}895$ and 2,055 °C with layer thicknesses of 25–30 nm. The solar cells for the ITO development were deposited with nc-SiC:H(n) layers deposited at $T_f = 1{,}775$ °C with a thickness of 3 nm, followed by $T_f = 1{,}950$ °C with a thickness of 30 nm.

For solar cells, the back side SiO₂ was removed in a hydrofluoric acid dip for 5 min following SiC deposition. Afterwards, the a-Si:H(i) 7 nm and a-Si:H(p) 7.4 nm layers were deposited at 200 °C in an AK1000 PECVD system provided by Meyer Burger. The intrinsic layer was deposited at 50 W with an H₂ flow of 650 sccm and a SiH₄ flow of 145 sccm. The p-type layer was deposited at 90 W with an H₂ flow of 500 sccm, a SiH₄ flow of 50 sccm and 1% trimethylboron in H₂ flow of 100 sccm. In this system, all back contacts for each solar cell experiment were deposited at once. The ITO was sputtered from a 3% ITO target rotating at 10 r.p.m. at a sample heater temperature of 250 °C and through a mask to create four 2×2 cm² solar cells on each wafer. The ITO on the a-Si:H(p) was sputtered, using a deposition pressure of 6 μbar, deposition power of 5 kW, an Ar flow of 90 sccm and an O₂ flow of 5 sccm. The ITO deposition of the back side was kept the same throughout this study. For sputtering on the nc-SiC:H(n) the reference ITO was deposited at a deposition pressure of 6 μbar, deposition power of 5 kW, an Ar flow of 197 sccm and an O₂ flow of 3 sccm. In the ITO optimization experiment for the n-side, deposition pressures of 10, 15 and 20 μbar and deposition powers of 0.5, 3.35 and 6.2 kW are tested. The metal contacts have been screen printed by an MT-650TVC screen printer from Micro-tec using a low-temperature silver paste H9481 provided by NAMICS. The silver paste was afterwards annealed at 190 °C in an oven for 40 min. The curing of the solar cells was performed on a hot plate at 220 °C for 10 + 10 min. A MgF₂ ARC (125 nm) was thermally evaporated by an electron beam as an ARC on the front side of the best solar cell. The cell was subsequently annealed for 10 min on a hot plate at 200 °C. The oxygen plasma treatment of the sample covered with UV filters was done in an Oxford Instruments OpAL ALD reactor for 15 min. The O₂ flow was 100 sccm at 0.12 mbar and 300 W at 50 °C. The respective ITO deposition was performed at 3.35 kW and 15 μbar.

DoE for double layer stack development of nc-SiC:H(n). To be able to judge which HWCVD deposition parameter has a significant influence on the device performance, we varied five parameters on two levels (high and low). We varied the filament temperature (and thereby the conductivity) of the nc-SiC:H(n) deposition as well as the layer thickness for the passivation and the conductive layer separately. The filament temperature was changed from 1,775 to 1,875 °C and from 1,950 to 2,060 °C for the passivation and the conductive nc-SiC:H(n) layer, respectively. The layer thickness was changed from 3 to 13 nm and from 11 to 27 nm for the passivation and conductive layer, respectively. The wire temperature was measured using a Raytek Marathon pyrometer with an accuracy

of approximately ±20 °C. The layer thickness is estimated from thickness measurements of nc-SiC:H(n) on polished silicon substrates. The doping gas flow rate of nitrogen was kept the same for both layers but was varied between 30 and 100 sccm. If all parameter combinations were to be investigated that would result in a total number of 32 experiments. Therefore, we decided to use the advantage of a fractional factorial plan that allowed us to reduce the experiments to 16. Additionally, we did three centre-point experiments (experiments 17–19 in Supplementary Table 1) where all five parameters had the centre value between high and low levels to judge the significance of the parameters. Nevertheless, by this reduction in number of experiments we sacrificed complete information about all interactions of the deposition parameters. To be able to see the influences of the five parameters we calculated the effect E of each parameter i: $E_i = \bar{y}_{high} - \bar{y}_{low}$ where $\bar{y}_{high}$ is the mean value of the results y when the parameter was set to the high level and $\bar{y}_{low}$ is the mean value of the results y when the parameter was set to the low level. The result hereby means the measured value by current–voltage (IV) or photoconductance measurements (for example, efficiency, fill factor or iV_{oc}). The stronger the absolute effect is, the stronger is the influence of the investigated parameter on the final result. When the effect is positive, changing the level of the parameter from low to high results in an increase of y.

In the case of the effect of the passivation layer thickness on the fill factor as shown in Supplementary Fig. 2, the effect is negative meaning that the fill factor can be increased by decreasing the layer thickness. If the output parameter should be decreased to increase the efficiency of the final device as is the case for the series resistance (Supplementary Fig. 3), a parameter with a positive effect should be set to its low value to decrease the series resistance.

To evaluate the significance of each effect, we computed the pure error, PE, from the variance, V_{cp}, of the results for the three centre-point experiments.

$$PE = \sqrt{\frac{4V_{cp}}{n}}$$

where n is the number of experiments excluding the centre points (for this DoE, $n = 16$). PE is then multiplied with the t value of Student's distribution with the confidence level α and the degrees of freedom, d.f. (for this DoE, 2)

Threshold $= PE \times t\left(\frac{\alpha+1}{2}, \text{d.f.}\right)$

The threshold is marked by a dashed line in the Supplementary Figs. 2–5 to visualize whether an effect is significant or not. If an effect lays within the grey area not exceeding the threshold, the effect has no significant influence on the result of the experiment.

Characterization of passivation quality. The passivation quality of the layer was tested on symmetric samples and solar cells before ITO deposition by measuring the photo-conductance of the wafer using a Sinton WCT-120 lifetime tester. From these measurements, the implied open-circuit voltage (iV_{oc}) at one sun, the saturation current density (J_0) at an excess charge carrier density of 5×10^{15} cm^{-3} and the effective minority charge carrier lifetime (τ_{eff}) at a charge carrier density of 1×10^{15} cm^{-3} were extracted[47,48].

SIMS measurement. The SIMS (time-of-flight-SIMS IV by IONTOF) measurement was conducted to analyse the interface properties of the nc-SiC:H(n)/SiO$_2$/c-Si(n) stack, to investigate the correlation between passivation quality and filament temperature. An area of 300×300 μm^2 was sputtered (using a 1 keV Cs ion beam), and an area of approximately 80×80 μm^2 was measured (using a 30 keV Bi1 ion beam).

STEM and energy dispersive X-ray measurements. The high-resolution bright-field STEM images were obtained with a probe aberration corrected Hitach HF5000 microscope. EDX mapping of the O-K edge, Si-L edge and C-K edge were obtained at the aberration corrected FEI Titan G2 80-200 microscope equipped with a four-quadrant EDX detector. The sample for STEM measurement and EDX mapping was prepared from the same batch of double nc-SiC:H(n) layer stack as that for SIMS measurement.

UV photoelectron spectroscopy (UPS) measurement. The UPS system is a MULTIPROBE MXPS system from Scienta Omicron with an ARGUS hemispherical electron spectrometer and part of the JOSEPH cluster system in the Research Center Jülich. The light source for UPS measurements is a HIS13 HeI gas discharge vacuum UV source from FOCUS (main line HeIα 21.22 eV). Spectra are collected with a path energy of 2 eV, a digital resolution of 0.01 eV and a sample bias of 6 V at a takeoff angle of 0°. Since we suspected the absolute positions of the spectral features were influenced by sample charging, we only determined the ionization energy E_i from the distance of the cutoff at low kinetic energies and the valence band edge at high kinetic energies by linear fits to the spectrum. The measurements were averaged over four positions on the sample.

Characterization of contact resistivity and IV characteristics. The contact resistivity (ρ_c) was measured on an in-house setup using the TLM. The contact resistivity was evaluated for the complete front side layer stack of c-Si(n)/TPC/ITO/Ag. The efficiency, the fill factor, the open-circuit voltage and the short-circuit

current density were measured by IV measurements under standard test conditions using the LOANA system from pv-tools. The series resistance was derived from J_{sc}–V_{oc} measurement[49].

UV degradation experiment. For the UV degradation experiment, different UV filters were used to find the energy range in which the light has the ability to degrade the surface passivation. Therefore, the three filters had different transmission properties for the light. The transmission properties are summarized in Supplementary Table 2. For the experiment with oxygen plasma (Supplementary Fig. 14c), a thicker filter (5 mm) was used as compared to the ITO sputter experiment (Supplementary Fig. 14d). Thus, the thinner filter has a higher typical transmission.

Photoluminescence measurement. The lifetime-corrected photoluminescence images were taken using a Xenics Cheetah 640-CL InGaAs camera cooled to 0 °C. To obtain a lifetime-corrected photoluminescence image, four images have to be taken during one illumination cycle. The method to calculate the lifetime-photoluminescence image from the four photoluminescence images taken during one illumination cycle is described in literature[50,51]. The lifetime-photoluminescence image is corrected afterwards for the effective minority charge carrier lifetime measured by photo-conductance. A general description of the underlying physical principles of photoluminescence is described elsewhere[52].

Simulations. Electrical simulations based on the optimized TPC solar cells were performed using TCAD Sentaurus with parameters of c-Si(n) and amorphous layers as reported in ref. [43]. The simulations used measured electronic parameters of our conductive and passivating nc-SiC:H(n) layers. More details of the parameters can be found in the Supplementary Information (Supplementary Discussion 2 and Supplementary Tables 3 and 4). Optical simulations based on the optimized TPC solar cells were performed using GenPro4 (ref. [37]). The simulations were based on double-side textured interfaces with layers' measured thicknesses and complex refractive indices. More details of the parameters can be found in the Supplementary Information (Supplementary Table 5 and Supplementary Fig. 21).

Reporting Summary. Further information on research design is available in the Nature Research Reporting Summary linked to this article.

Data availability
All data generated or analysed during this study are included in the published article and its Supplementary Information. Source data are provided with this paper.

References
1. Min, B. et al. A roadmap toward 24% efficient PERC solar cells in industrial mass production. *IEEE J. Photovolt.* **7**, 1541–1550 (2017).
2. Wakisaka, K. et al. More than 16% solar cells with a new 'HIT' (doped a-Si/nondoped a-Si/crystalline Si) structure. In *Proc. Conference Record of the Twenty-Second IEEE Photovoltaic Specialists Conference* 887–892 (IEEE, 1991); https://doi.org/10.1109/PVSC.1991.169337
3. Tanaka, M. et al. Development of a new heterojunction structure (ACJ-HIT) and its application to polycrystalline silicon solar cells. *Prog. Photovolt. Res. Appl.* **1**, 85–92 (1993).
4. Masuko, K. et al. Achievement of more than 25% conversion efficiency with crystalline silicon heterojunction solar cell. *IEEE J. Photovolt.* **4**, 1433–1435 (2014).
5. Peibst, R. et al. Working principle of carrier selective poly-Si/c-Si junctions: is tunnelling the whole story? *Sol. Energy Mater. Sol. Cells* **158**, 60–67 (2016).
6. Feldmann, F., Bivour, M., Reichel, C., Hermle, M. & Glunz, S. W. Passivated rear contacts for high-efficiency n-type Si solar cells providing high interface passivation quality and excellent transport characteristics. *Sol. Energy Mater. Sol. Cells* **120**, 270–274 (2014).
7. Battaglia, C. et al. Hole selective MoO$_x$ contact for silicon solar cells. *Nano Lett.* **14**, 967–971 (2014).
8. Geissbühler, J. et al. 22.5% efficient silicon heterojunction solar cell with molybdenum oxide hole collector. *Appl. Phys. Lett.* **107**, 081601 (2015).
9. Bullock, J. et al. Efficient silicon solar cells with dopant-free asymmetric heterocontacts. *Nat. Energy* **1**, 15031 (2016).
10. Yang, X. et al. Dual-function electron-conductive, hole-blocking titanium nitride contacts for efficient silicon solar cells. *Joule* **3**, 1314–1327 (2019).
11. Dréon, J. et al. 23.5%-efficient silicon heterojunction silicon solar cell using molybdenum oxide as hole-selective contact. *Nano Energy* **70**, 104495 (2020).
12. Feldmann, F., Nicolai, M., Müller, R., Reichel, C. & Hermle, M. Optical and electrical characterization of poly-Si/SiO$_x$ contacts and their implications on solar cell design. *Energy Procedia* **124**, 31–37 (2017).

13. Köhler, M. et al. Development of a transparent passivated contact as a front side contact for silicon heterojunction solar cells. In *Proc. 2018 IEEE 7th World Conference on Photovoltaic Energy Conversion (WCPEC)* 3468–3472 (IEEE, 2018); https://doi.org/10.1109/PVSC.2018.8548008

14. Köhler, M. et al. Optimization of transparent passivating contact for crystalline silicon solar cells. *IEEE J. Photovolt.* **10**, 46–53 (2020).

15. Pomaska, M. *Microcrystalline Silicon Carbide for Silicon Heterojunction Solar Cells*. PhD thesis, RWTH Aachen Univ. (2017).

16. Umemoto, H. et al. Direct detection of H atoms in the catalytic chemical vapor deposition of the SiH_4/H_2 system. *J. Appl. Phys.* **91**, 1650–1656 (2002).

17. Irikawa, J., Miyajima, S., Watahiki, T. & Konagai, M. High efficiency hydrogenated nanocrystalline cubic silicon carbide/crystalline silicon heterojunction solar cells using an optimized buffer layer. *Appl. Phys. Express* **4**, 092301 (2011).

18. Pomaska, M., Beyer, W., Neumann, E., Finger, F. & Ding, K. Impact of microcrystalline silicon carbide growth using hot-wire chemical vapor deposition on crystalline silicon surface passivation. *Thin Solid Films* **595**, 217–220 (2015).

19. Ingenito, A. et al. A passivating contact for silicon solar cells formed during a single firing thermal annealing. *Nat. Energy* **3**, 800–808 (2018).

20. Qiu, K. et al. Development of conductive SiC_x:H as a new hydrogenation technique for tunnel oxide passivating contacts. *ACS Appl. Mater. Interfaces* **12**, acsami.0c06637 (2020).

21. Liu, W. et al. Polysilicon passivating contacts for silicon solar cells: interface passivation and carrier transport mechanism. *ACS Appl. Energy Mater.* **2**, 4609–4617 (2019).

22. Glunz, S. W. & Feldmann, F. SiO_2 surface passivation layers—a key technology for silicon solar cells. *Sol. Energy Mater. Sol. Cells* **185**, 260–269 (2018).

23. Cuevas, A. et al. Carrier population control and surface passivation in solar cells. *Sol. Energy Mater. Sol. Cells* **184**, 38–47 (2018).

24. Procel, P., Yang, G., Isabella, O. & Zeman, M. Theoretical evaluation of contact stack for high efficiency IBC-SHJ solar cells. *Sol. Energy Mater. Sol. Cells* **186**, 66–77 (2018).

25. Procel, P., Yang, G., Isabella, O. & Zeman, M. Numerical simulations of IBC solar cells based on poly-Si carrier-selective passivating contacts. *IEEE J. Photovolt.* **9**, 374–384 (2019).

26. Pomaska, M. et al. Role of oxygen and nitrogen in n-type microcrystalline silicon carbide grown by hot wire chemical vapor deposition. *J. Appl. Phys.* **120**, 225105 (2016).

27. Demaurex, B., De Wolf, S., Descoeudres, A., Charles Holman, Z. & Ballif, C. Damage at hydrogenated amorphous/crystalline silicon interfaces by indium tin oxide overlayer sputtering. *Appl. Phys. Lett.* **101**, 171604 (2012).

28. Morales-Vilches, A. B. et al. ZnO:Al/a-SiO_x front contact for polycrystalline-silicon-on-oxide (POLO) solar cells. In *Proc. 8th International Conference on Crystalline Silicon Photovoltaics* 040016 (2018); https://doi.org/10.1063/1.5049279

29. Tutsch, L. et al. Implementing transparent conducting oxides by DC sputtering on ultrathin SiO_x/poly-Si passivating contacts. *Sol. Energy Mater. Sol. Cells* **200**, 109960 (2019).

30. Illiberi, A., Kudlacek, P., Smets, A. H. M., Creatore, M. & van de Sanden, M. C. M. Effect of ion bombardment on the a-Si:H based surface passivation of c-Si surfaces. *Appl. Phys. Lett.* **98**, 242115 (2011).

31. Profijt, H. B., Kudlacek, P., van de Sanden, M. C. M. & Kessels, W. M. M. Ion and photon surface interaction during remote plasma ALD of metal oxides. *J. Electrochem. Soc.* **158**, G88–G91 (2011).

32. Reed, M. L. & Plummer, J. D. Chemistry of Si–SiO_2 interface trap annealing. *J. Appl. Phys.* **63**, 5776–5793 (1988).

33. Mazzarella, L. et al. p-type microcrystalline silicon oxide emitter for silicon heterojunction solar cells allowing current densities above $40\,mA/cm^2$. *Appl. Phys. Lett.* **106**, 023902 (2015).

34. Herasimenka, S. Y., Dauksher, W. J., Boccard, M. & Bowden, S. ITO/SiO_x:H stacks for silicon heterojunction solar cells. *Sol. Energy Mater. Sol. Cells* **158**, 98–101 (2016).

35. Adachi, D., Hernández, J. L. & Yamamoto, K. Impact of carrier recombination on fill factor for large area heterojunction crystalline silicon solar cell with 25.1% efficiency. *Appl. Phys. Lett.* **107**, 233506 (2015).

36. Hernández, J. L. et al. High efficiency silver-free heterojunction silicon solar cell. *Jpn. J. Appl. Phys.* **51**, 10NA04 (2012).

37. Santbergen, R. et al. GenPro4 optical model for solar cell simulation and its application to multijunction solar cells. *IEEE J. Photovolt.* **7**, 919–926 (2017).

38. Huang, Y. et al. Preparation of microcrystalline silicon solar cells on microcrystalline silicon carbide window layers grown with HWCVD at low temperature. *J. Non Cryst. Solids* **354**, 2430–2434 (2008).

39. Zhang, D. et al. Design and fabrication of a SiO_x/ITO double-layer anti-reflective coating for heterojunction silicon solar cells. *Sol. Energy Mater. Sol. Cells* **117**, 132–138 (2013).

40. Santbergen, R. et al. Minimizing optical losses in monolithic perovskite/c-Si tandem solar cells with a flat top cell. *Opt. Express* **24**, A1288 (2016).

41. Richter, A., Hermle, M. & Glunz, S. W. Reassessment of the limiting efficiency for crystalline silicon solar cells. *IEEE J. Photovolt.* **3**, 1184–1191 (2013).

42. Khanna, A. et al. A fill factor loss analysis method for silicon wafer solar cells. *IEEE J. Photovolt.* **3**, 1170–1177 (2013).

43. Procel, P. et al. The role of heterointerfaces and subgap energy states on transport mechanisms in silicon heterojunction solar cells. *Prog. Photovolt. Res. Appl.* **28**, 935–945 (2020).

44. Römer, U. et al. Recombination behavior and contact resistance of n+ and p+ poly-crystalline Si/mono-crystalline Si junctions. *Sol. Energy Mater. Sol. Cells* **131**, 85–91 (2014).

45. Kern, W. The evolution of silicon wafer cleaning technology. *J. Electrochem. Soc.* **137**, 1887–1892 (1990).

46. Köhler, M. et al. Wet-chemical preparation of silicon tunnel oxides for transparent passivated contacts in crystalline silicon solar cells. *ACS Appl. Mater. Interfaces* **10**, 14259–14263 (2018).

47. Sinton, R. A., Cuevas, A. & Stuckings, M. Quasi-steady-state photoconductance, a new method for solar cell material and device characterization. In *Proc. Conference Record of the Twenty Fifth IEEE Photovoltaic Specialists Conference* 457–460 (IEEE, 1996); https://doi.org/10.1109/PVSC.1996.564042

48. Kimmerle, A., Rothhardt, P., Wolf, A. & Sinton, R. A. Increased reliability for J_0-analysis by QSSPC. *Energy Procedia* **55**, 101–106 (2014).

49. Aberle, A. G., Wenham, S. R. & Green, M. A. Series resistance of solar cells. In *Proc. Photovoltaic Specialists Conference* 133–139 (IEEE, 1993).

50. Ramspeck, K., Reissenweber, S., Schmidt, J., Bothe, K. & Brendel, R. Dynamic carrier lifetime imaging of silicon wafers using an infrared-camera-based approach. *Appl. Phys. Lett.* **93**, 102104 (2008).

51. Herlufsen, S. et al. Dynamic photoluminescence lifetime imaging for the characterisation of silicon wafers. *Phys. Status Solidi - Rapid Res. Lett.* **5**, 25–27 (2011).

52. Rau, U. Superposition and reciprocity in the electroluminescence and photoluminescence of solar cells. *IEEE J. Photovolt.* **2**, 169–172 (2012).

53. Green, M. A. Self-consistent optical parameters of intrinsic silicon at 300K including temperature coefficients. *Sol. Energy Mater. Sol. Cells* **92**, 1305–1310 (2008).

Author contributions

M.K., M.P. and K.Q. designed the experiments. M.K. carried out the layer and device fabrication and characterization including use of the ellipsometer, quasi-steady-state-photoconductance, transfer line method, photoluminescence, transmittance and reflectance, current–voltage and quantum efficiency. A.Z. contributed to the SiC deposition. A.L. and W.D. contributed to the a-Si:H, ITO and MgF_2 deposition and optimization, and optical properties measurements. B.M. contributed to TCO optimization. S.L., K.Q. and M.P. contributed to screen printing. A.Z and A.E. developed the curing of MgF_2. A.E. performed the SIMS measurements. P.C. and M.L. performed HRSTEM measurements and EDX mapping. B.K. performed UPS measurements. P.P., R.S. and O.I. executed the TCAD and GenPro4 simulation. M.K., M.P., K.Q., F.F., T.K., U.R. and K.D. contributed to the definition and presentation of the paper content. M.K., M.P., K.Q. and K.D. organized the research. M.P., F.F., U.R., K.D. and M.K. developed the concept of TPC by specific layer stack. M.K., K.Q., T.K. and U.R. wrote the paper, and all other authors discussed the results and proofread the paper.

Competing interests

The authors declare no competing interests.

Additional information

Supplementary information The online version contains supplementary material available at https://doi.org/10.1038/s41560-021-00806-9.

Correspondence and requests for materials should be addressed to M.K., M.P., K.Q. or K.D.

Peer review information *Nature Energy* thanks the anonymous reviewers for their contribution to the peer review of this work.

Reprints and permissions information is available at www.nature.com/reprints.

Publisher's note Springer Nature remains neutral with regard to jurisdictional claims in published maps and institutional affiliations.

nature research

Corresponding author(s):   Malte Köhler, Manuel Pomaska, Kaifu Qiu, Kaining Ding

Solar Cells Reporting Summary

Nature Research wishes to improve the reproducibility of the work that we publish. This form is intended for publication with all accepted papers reporting the characterization of photovoltaic devices and provides structure for consistency and transparency in reporting. Some list items might not apply to an individual manuscript, but all fields must be completed for clarity.

For further information on Nature Research policies, including our data availability policy, see Authors & Referees.

▶ Experimental design

Please check: are the following details reported in the manuscript?

1. Dimensions

   Area of the tested solar cells
   ☒ Yes ☐ No
   20x20 mm2

   Method used to determine the device area
   ☒ Yes ☐ No
   A transparent conducting oxide was sputtered through a mask to define the cell area.

2. Current-voltage characterization

   Current density-voltage (J-V) plots in both forward and backward direction
   ☐ Yes ☒ No
   The same J-V results are obtained for our silicon solar cells when changing the scanning direction.

   Voltage scan conditions
   For instance: scan direction, speed, dwell times
   ☒ Yes ☐ No
   Scan direction: positive to negative, with 88 data points between -0.1 V and +0.744 V.

   Test environment
   For instance: characterization temperature, in air or in glove box
   ☐ Yes ☒ No
   The measurements are performed in air on a calibrated measurement system under standard test conditions.

   Protocol for preconditioning of the device before its characterization
   ☐ Yes ☒ No
   No protocol applies to the preconditioning of silicon solar cells.

   Stability of the J-V characteristic
   Verified with time evolution of the maximum power point or with the photocurrent at maximum power point; see ref. 7 for details.
   ☐ Yes ☒ No
   The J-V characteristic was stable over time also when measured again after several weeks.

3. Hysteresis or any other unusual behaviour

   Description of the unusual behaviour observed during the characterization
   ☐ Yes ☒ No
   Our cells did not show any unusual behavior or hysteresis.

   Related experimental data
   ☐ Yes ☒ No
   Our cells did not show any unusual behavior or hysteresis.

4. Efficiency

   External quantum efficiency (EQE) or incident photons to current efficiency (IPCE)
   ☒ Yes ☐ No
   Presented in the supporting information Supplementary Figure 18.

   A comparison between the integrated response under the standard reference spectrum and the response measure under the simulator
   ☒ Yes ☐ No
   Comparison was performed within the certification procedure.

   For tandem solar cells, the bias illumination and bias voltage used for each subcell
   ☐ Yes ☒ No
   We do not report on tandem cells.

5. Calibration

   Light source and reference cell or sensor used for the characterization
   ☒ Yes ☐ No
   AAA Loana Sun Simulator by pv-tools GmbH including a reference cell with a Sinus-220 LED light source by WAVELABS Solar Metrology Systems GmbH.

   Confirmation that the reference cell was calibrated and certified
   ☒ Yes ☐ No
   Reference cell was calibrated by pv-tools using a silicon solar cell calibrated at Physikalisch-Technische Bundesanstalt at Braunschweig Germany.

| Calculation of spectral mismatch between the reference cell and the devices under test | ☒ Yes ☐ No | Spectral missmatch is calculated using a calibrated reference cell. For certified solar cells the spectral missmatch is calculated using IEC 60904-7. |

6. Mask/aperture

| Size of the mask/aperture used during testing | ☒ Yes ☐ No | 3.61 cm2 for in-house measurements, (3.487 ± 0.017) cm2 for calibration. |

| Variation of the measured short-circuit current density with the mask/aperture area | ☐ Yes ☒ No | No variation expected due to homogeneity of the solar cells. |

7. Performance certification

| Identity of the independent certification laboratory that confirmed the photovoltaic performance | ☒ Yes ☐ No | ISFH CalTeC D-K-18657-01-00 |

| A copy of any certificate(s)
Provide in Supplementary Information | ☒ Yes ☐ No | Results are presented in supplementary information Supplementary Figure 17 and 19. |

8. Statistics

| Number of solar cells tested | ☒ Yes ☐ No | Each wafer contains 4 nominally identical solar cells. |

| Statistical analysis of the device performance | ☒ Yes ☐ No | Boxplots are used to show the statistics. |

9. Long-term stability analysis

| Type of analysis, bias conditions and environmental conditions
For instance: illumination type, temperature, atmosphere humidity, encapsulation method, preconditioning temperature | ☒ Yes ☐ No | Remeasuring the cells after several weeks in air lead to the same results. |